Journal of Molecular Catalysis A: Chemical 408 (2015) 138–146

Contents lists available at ScienceDirect

Journal of Molecular Catalysis A: Chemical

journal homepage: www.elsevier.com/locate/molcata

# Carbon supported gold and silver: Application in the gas phase hydrogenation of *m*-dinitrobenzene

Fernando Cárdenas-Lizana[a], Zahara M. De Pedro[a,1], Santiago Gómez-Quero[a,2], Lioubov Kiwi-Minsker[b], Mark A. Keane[a,*]

[a] Chemical Engineering, School of Engineering and Physical Sciences, Heriot Watt University, Edinburgh EH14 4AS Scotland, UK
[b] Group of Catalytic Reaction Engineering, Ecole Polytechnique Fédérale de Lausanne (GGRC-ISIC-EPFL), Lausanne CH-1015, Switzerland

ARTICLE INFO

*Article history:*
Received 10 June 2015
Received in revised form 13 July 2015
Accepted 14 July 2015
Available online 23 July 2015

*Keywords:*
Selective gas phase hydrogenation
*m*-Dinitrobenzene
Functionalised activated carbon
Au/AC
Ag/AC

ABSTRACT

We have studied the gas phase continuous hydrogenation of *m*-dinitrobenzene (*m*-DNB) over acid treated activated carbon (AC) supported Au and Ag prepared by deposition-precipitation. Temperature programmed reduction of a 1%wt. metal loading generated a broad distribution of Au (mean = 45 nm) and Ag (mean = 13 nm) nanoparticles. A decrease in metal content to 0.1%wt. served to increase dispersion (Au/AC (mean = 4 nm) and Ag/AC (mean = 3 nm)) where both catalysts exhibited an electron enriched (from XPS) metal phase. *m*-DNB hydrogenation activity was stable with time on-stream where partial hydrogenation (to *m*-nitroaniline (*m*-NAN)) was favoured at low conversion with a switch to full hydrogenation (to *m*-phenylenediamine (*m*-PDM)) at higher conversions consistent with a stepwise reaction mechanism. Reaction over 0.1%wt. Au/AC delivered a greater than 5-fold higher turnover frequency (*TOF*) relative to Ag/AC that can be attributed to a higher $H_2$ chemisorption capacity under reaction conditions. Activation energy for *m*-DNB → *m*-NAN was the same (110 kJ $mol^{-1}$) for both catalysts. We have established differences in the conversion/selectivity response where *m*-NAN formation was enhanced over Ag/AC at the same conversion, which is ascribed to differences in *m*-DNB adsorption/activation.

## 1. Introduction

The selective hydrogenation of nitroarenes to aromatic amines continues to attract significant research due to its industrial relevance [1]. Exclusive -$NO_2$ group reduction is difficult to achieve in the presence of other reactive functionalities such as carbonyl, cyano, alkenyl or halogen groups [2]. The focus has moved from conventional Fe promoted reduction in acid media (Béchamp process) [3] to the application of transition metal (*e.g.* Pd [4], Pt [5]) catalysts. In previous work, we demonstrated the potential of oxide supported Au and Ag to promote the chemoselective reduction of funtionalised nitroarenes [6] and established a nucleophilic reaction mechanism [7]. Oxides have been the most widely used Au and Ag carriers where support surface chemistry (*e.g.* Lewis acidity-basicity) can impact on hydrogenation performance [8,9]. Carbon offers a number of advantages over oxide supports, notably cost effectiveness, stability in acid and base media and the possibility of adjusting porosity, specific surface area (SSA > 600 $m^2\,g^{-1}$) and surface chemistry for specific catalytic applications [10]. The application of carbon supported Au or Ag catalysts in hydrogen mediated reactions has been explored to a limited extent. Published work has primarily dealt with Pd-containing bimetallics where Au [11–13] and Ag [14] were shown to influence selectivity in liquid [11,12,14] and gas [13] phase conversion of cinnamaldehyde [11,12], carbon tetrachloride [14] and tetrachloromethane [13]. We should also note literature that has reported enhanced activity and selectivity in hydrogenation (1,3-butadiene [15], cinnamaldehyde [15], *o*-, *m*- and *p*-chloronitrobenzenes and nitrobenzaldehydes [16]), hydrodechlorination (carbon tetrachloride [17]) and hydrodeoxygenation (vanillin [18]) over (carbon nanotube [15,18] and $C_{60}$ [16]) supported Au [15,18] and Ag [16,17].

We could not find any publication that has provided a direct comparison of the catalytic performance of carbon supported Au and Ag. This may be due, in part, to difficulties in preparing well dispersed (≤10 nm) Au and Ag particles on carbonaceous carriers [19], which is critical for significant hydrogenation activity [2,6]. The catalytic response in the production of functionalised anilines

---

[*] Corresponding author.
*E-mail address:* M.A.Keane@hw.ac.uk (M.A. Keane).

[1] Current address: Ingeniería Química, Facultad de Ciencias, Universidad Autónoma de Madrid, Cantoblanco, 28049 Madrid, Spain.

[2] Current address: Avantium, Zekeringstraat 29, Amsterdam 1014 BV, The Netherlands.

http://dx.doi.org/10.1016/j.molcata.2015.07.019

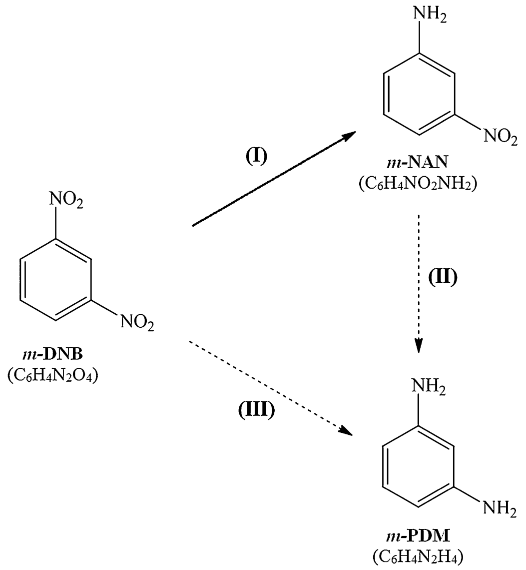

**Scheme 1.** Reaction pathways in the partial hydrogenation of *m*-dinitrobenzene (*m*-DNB) to *m*-nitroaniline (*m*-NAN, solid line) and full hydrogenation to *m*-phenylenediamine (*m*-PDM, dashed lines).

can be controlled by contributions due to metal size and electronic character which, in turn, are dependent on metal loading [20], method of synthesis and support interactions [21]. Carbon carriers are intrinsically hydrophobic and hydrophilic properties are required to increase surface wettability by polar solvents (*e.g.* water) and facilitate homogeneous distribution of supported metal precursor(s) [22]. Surface oxygen-containing functionalities (i) act as metal-anchoring sites [22], (ii) promote reduction of the metal precursor [23] and (iii) lower hydrophobicity and improve support accessibility during catalyst synthesis [10]. The concentration and nature of surface groups can be tailored by treatment with oxidising agents ($HNO_3$, $KMnO_4$, $H_2SO_4/HNO_3$, $(NH_4)_2S_2O_8$, $H_2O_2$, and $O_3$) [24].

In this work, we compare the performance of activated carbon (AC) supported Au and Ag in the gas phase hydrogenation of *m*-dinitrobenzene (*m*-DNB). Products of partial (*m*-nitroaniline (*m*-NAN)) and complete (*m*-phenylenediamine (*m*-PDM)) reduction (see Scheme 1) find multiple use in the manufacture of polymers and dyes [25,26] where selective formation of *m*-NAN or *m*-PDM is challenging. We address the feasibility of controlling product distribution by modifying the size and electronic properties of the supported metal phase through variations in metal loading and support interactions.

## 2. Experimental

### 2.1. Materials and analytical methods

The *m*-DNB reactant (Sigma–Aldrich, ≥98%) and solvent (1-butanol, Riedel-de Häen, ≥99.5%) were used as supplied, without further purification. All gases ($H_2$, $N_2$, Ar, $O_2$ and He) were of ultra-high purity (BOC, >99.99%). The composition of the reaction/product mixtures was determined using a PerkinElmer Auto System XL gas chromatograph (GC) equipped with a programmed split/splitless injector and a flame ionisation detector, employing a DB-1 50 m × 0.20 mm i.d., 0.33 μm film thickness capillary column (J&W Scientific). Data acquisition and manipulation were performed using the TotalChrom Workstation chromatography data system. Reactant and product molar fractions ($x_i$) were obtained from detailed calibration plots (not shown) and carbon mass balance was within ±5%. The degree of nitro-group reduction ($X_{-\mathrm{NO}_2}$) is given by

$$X_{-\mathrm{NO}_2} = \frac{[-\mathrm{NH}_2]_{\mathrm{out}}}{[-\mathrm{NO}_2]_{\mathrm{in}}} = \frac{2 \times [m-\mathrm{PDM}]_{\mathrm{out}} + [m-\mathrm{NAN}]_{\mathrm{out}}}{2 \times [m-\mathrm{DNM}]_{\mathrm{in}}} \tag{1}$$

where [*m*-DNB], [*m*-NAN] and [*m*-PDM] are, respectively, the concentrations of *m*-dinitrobenzene, *m*-nitroaniline and *m*-phenylenediamine; subscripts *in* and *out* refer to inlet and outlet streams. Reactant fractional conversion ($X_{m\text{-DNB}}$) is defined by

$$X_{m-\mathrm{DNB}} = \frac{[m-\mathrm{DNB}]_{\mathrm{in}} - [m-\mathrm{DNB}]_{\mathrm{out}}}{[m-\mathrm{DNB}]_{\mathrm{in}}} \tag{2}$$

and selectivity in terms of (for example) *m*-NAN ($S_{m\text{-NAN}}$) is given by

$$S_{m-\mathrm{NAN}} = \frac{[m-\mathrm{NAN}]_{\mathrm{out}}}{[m-\mathrm{DNB}]_{\mathrm{in}} - [m-\mathrm{DNB}]_{\mathrm{out}}} \tag{3}$$

Repeated reactions with the same batch of catalyst delivered conversion/selectivity values that were reproducibility to better than ±6%.

### 2.2. Catalyst preparation and activation

The AC support was obtained from NORIT (UK) and subjected to demineralisation by treatment with HF ($100\,\mathrm{cm}^3\,\mathrm{g}^{-1}$). The support was then refluxed in $HNO_3 + H_2SO_4$ (1:1 v/v, $20\,\mathrm{cm}^3\,\mathrm{g}^{-1}$) for 1 h to introduce surface oxygen groups [24]. Carbon supported Au and Ag (1% and 0.1%wt.) were prepared by deposition-precipitation using urea as basification agent which has been shown to generate nano-sized (<5 nm) Au [4] and Ag [27]. Aqueous urea (100 times excess) and $HAuCl_4$ ($5 \times 10^{-4}$ M, $300\,\mathrm{cm}^3$) or $AgNO_3$ ($5 \times 10^{-4}$ M, $300\,\mathrm{cm}^3$) was added to the AC support (5 g). The pH was continuously monitored using a crystal-body pH electrode (Hanna Instruments) coupled to a data collection system (Pico Technology Ltd.). The suspension was heated to 353 K under constant agitation (300 rpm) with a pH increase due to the thermal decomposition of urea [28]. The solid catalyst obtained was washed repeatedly with deionized water until chlorine free (based on the $AgNO_3$ test) and dried in He ($60\,\mathrm{cm}^3\,\mathrm{min}^{-1}$) at 383 K for 3 h. Samples were sieved to 75 μm average particle diameter (ATM fine test sieves) and stored at 277 K in the dark. Catalyst activation by temperature programmed reduction (TPR) employed a $2\,\mathrm{K\,min}^{-1}$ ramp to 623 K in $60\,\mathrm{cm}^3\,\mathrm{min}^{-1}$ $H_2$. The temperature requirements for reduction of supported Au and Ag precursors have been discussed elsewhere [7,29]. Post-activation the samples were cooled to ambient temperature and passivated in 1% v/v $O_2$/He for 1 h for *ex situ* characterisation.

### 2.3. Support and catalyst characterisation

The (Au and Ag) metal loading was determined by inductively coupled plasma-optical emission spectrometry (Vista-PRO, Varian Inc.) from the diluted extract of aqua regia. Acid/base titrations were performed by immersing 25 mg of sample in $50\,\mathrm{cm}^3$ solution of 0.1 M NaCl and 0.1 mM oxalic acid, acidified to pH 3 with HCl (0.1 M) with constant stirring in a He atmosphere. A 0.1 M NaOH solution was used as titrant, added dropwise ($3\,\mathrm{cm}^3\,\mathrm{h}^{-1}$) using a 100 Kd Scientific microprocessor-controlled infusion pump and the pH monitored as above. Acidity was quantified as the volume of NaOH required to neutralise surface groups where $\mathrm{p}K_{\mathrm{i}} \le 7$ [30]. Micro-Raman spectra of the support were recorded with a Renishaw Raman Microscope System RM1000 equipped with a Leica microscope, an electrically refrigerated CCD camera and a diode laser at 514 nm as excitation source operating at a power level of 3 mW. Total SSA and pore volume were determined by $N_2$ adsorption at 77 K using the Sorptomatic 1990 (Carlo Erba) system. Prior to analysis, samples were outgassed at 523 K for 2 h under vacuum ($<5 \times 10^{-2}$ Torr). Total pore volume was obtained from BJH analysis of the desorption isotherm. Hydrogen chemisorption (pulse 10 μl titration at 523 K) following TPR (in 17 $cm^3 min^{-1}$ (Brooks mass flow controlled) 5% v/v $H_2/N_2$ to 623 K at 2 $K min^{-1}$) and temperature programmed desorption (TPD in 65 $cm^3 min^{-1}$ $N_2$ to 873 K at 50 $K min^{-1}$) were conducted on the CHEM-BET 3000 (Quantachrome Instrument) unit with data acquisition/manipulation using the TPR Win$^{TM}$ software [20]. In a blank test, there was no measurable $H_2$ uptake on the AC support. Combined TCD calibrations with analysis of the effluent gas using a MICROMASS PC Residual Gas Analyzer confirmed that the TPD profiles can be ascribed solely to $H_2$ release. Powder X-ray diffractograms were recorded on a Bruker/Siemens D500 incident X-ray diffractometer using Cu Kα radiation. Samples were scanned at 0.02° $step^{-1}$ and the diffractograms identified using the JCPDS-ICDD reference standards (Au (04-0784) and Ag (04-0783)). Metal particle size ($d_{hkl}$) was estimated using the Scherrer equation:

$$d_{hkl} = \frac{K \times \lambda}{\beta \times \cos\theta} \tag{4}$$

where $K = 0.9$, λ is the incident radiation wavelength (1.54056 Å), β is the peak width at half the maximum intensity and $\theta$ represents the diffraction angle ($2\theta = 38.1°$) corresponding to the (1 1 1) plane for Au and Ag. Scanning electron microscopy (SEM) was conducted on a Philips FEI XL30-FEG with an Everhart-Thornley secondary-electron detector operated at an accelerating voltage of 10 kV and NORAN System SIX (version 1.6) for data analysis. The samples were subjected to decontamination using a plasma-cleaner (EVACTRON). Transmission electron microscopy (TEM) analysis was performed using a JEOL JEM 2011HRTEM unit with UTW energy dispersive X-ray detector (Oxford Instruments) at an accelerating voltage of 200 kV; data acquisition/manipulation employed Gatan DigitalMicrograph 3.4. Specimens were prepared by dispersion in acetone and deposited on a holey carbon/Cu grid (300 Mesh). Up to 1000 individual metal particles were counted for each catalyst and the surface area-weighted metal diameter ($d$) calculated from

$$d = \frac{\sum_i n_i d_i^3}{\sum_i n_i d_i^2} \tag{5}$$

where $n_i$ is the number of metal particles of diameter $d_i$. Analysis by X-ray photoelectron spectroscopy (XPS) employed an Axis Ultra instrument (Kratos Analytical) under ultra-high vacuum condition ($<10^{-8}$ Torr) with a monochromatic Al Kα X-ray source (1486.6 eV). The source power was maintained at 150 W and emitted photoelectrons were sampled from a $750 \times 350$ $\mu m^2$ area at a take-off angle = 90°. The analyser pass energy was 80 eV for survey spectra (0–1000 eV) and 40 eV for high resolution spectra (O 1*s*, Au $4f_{5/2}$, Au $4f_{7/2}$, Ag $3d_{3/2}$ and Ag $3d_{5/2}$). The adventitious carbon 1*s* peak at 284.5 eV was used as internal standard to compensate for charging effects. Spectra curve fitting and quantification were performed with the CasaXPS software using relative sensitivity factors provided by Kratos.

### 2.4. Catalysis procedure

Reactions were carried out under atmospheric pressure, *in situ* immediately after activation, in a fixed bed vertical continuous flow glass reactor ($l = 600$ mm, i.d. = 15 mm) over the temperature range $463 K \le T \le 573 K$ under conditions of minimal heat/mass transport limitations. A preheating zone (borosilicate glass beads) ensured that the *m*-DNB reactant was vaporised and reached reaction temperature before contacting the catalyst. Isothermal conditions (±1 K) were maintained by thoroughly mixing the catalyst with ground glass (75 μm). Temperature was continuously monitored by a thermocouple inserted in a thermowell within the catalyst bed. *m*-DNB was delivered as butanolic solutions in a co-current flow of $H_2$ *via* a glass/teflon air-tight syringe and teflon line using a microprocessor controlled infusion pump (Model 100 kd Scientific) at a fixed calibrated flow rate. Molar metal ($n$) to inlet $-NO_2$ feed rate ratio ($F$) spanned the range $1 \times 10^{-4}$–$1 \times 10^{-2}$ h. Hydrogen was far in excess of the stoichiometric requirements for the production of *m*-NAN and the flow rate was monitored using a Humonics (Model 520) digital flowmeter; $GHSV = 2 \times 10^4$ $h^{-1}$. Passage of *m*-DNB in $H_2$ through the empty reactor or over AC did not result in any detectable conversion.

## 3. Results and discussion

### 3.1. Sample characterisation

#### 3.1.1. Activated carbon (AC) support

Demineralisation of the AC support (in HF) served to remove residual metal impurities that could impact on the catalytic response [31]. Subsequent acid treatment (in $HNO_3 + H_2SO_4$) was used to introduce oxygen containing groups as nucleation sites for the deposition of Au and Ag [22]. A displacement of the acid-base titration curves for AC *pre*- and *post*-acid treatment (not shown) confirmed an increase in surface acidity due to the generation of carbonyl (quinone and lactone) and carboxyl (acid and anhydride) functionalities [32]. Acid-base titration delivered a pH at the equivalency point ($pK_a$) of 6.4, which suggests the absence of strong carboxylic acid sites ($pK_a < 5$) and the formation of surface quinone, lactone and anhydride groups [33]. The O 1*s* XPS signal provides information on surface functionalisation of carbon substrates [34]; the spectrum for acid treated AC is presented in Fig. 1(**I**).

After deconvolution, two near equivalent signals with BE = 531.2 eV and 533.3 eV are in evidence and can be attributed to carbonyl (quinone (531.1 eV) [35] and lactone (533.3 eV) [35]) and carboxyl anhydride (531.1 eV) [35] groups. The presence of these functionalities is consistent with the change in surface acidity inferred from titration. Activated carbon is characterised by a random arrangement of "basal planes", *i.e.* layers of interlocking aromatic rings [36]. The scanning electron microscopy images of acid treated AC (Fig. 1(**II**)) show heterogeneity in size (10–100 μm) and shape.

Raman spectroscopy measurement generated a profile (Fig. 1(**III**)) with two peaks attributable to the D- (1354 $cm^{-1}$, defects and/or curvature [37,38]) and G- (1600 $cm^{-1}$, ordered structure [39]) bands for carbonaceous materials. The relative intensity of these bands ($I_D/I_G$) serves as an index to evaluate graphitic character where the measured $I_D/I_G$ (=0.90) is within the range (0.73–1.26) reported for AC [40,41], higher than graphite (0.61 [40]) and consistent with an amorphous structure. Nitrogen adsorption/desorption isotherms are presented in Fig. 1(**IV**) where the associated SSA and total pore volume (Table 1) are in accord with values in the literature (349–884 $m^2 g^{-1}$; 0.19–0.58 $cm^3 g^{-1}$) [40,42]. The sharp increase in $N_2$ adsorption at low relative pressures ($P/P_0 \le 0.15$) and lesser uptake at higher $P/P_0$ suggest a type I IUPAC classification [43]. The distribution of pore diameters is shown in the inset to Fig. 1(**IV**)) with a calculated mean of 4.5 nm.

#### 3.1.2. Activated carbon supported Au and Ag

The metal loadings (Table 1) coincided with nominal values, a result that demonstrates the efficiency of the synthesis methodology. The TPR profiles (to 623 K, not shown) for 1 and 0.1%wt. Au/AC and Ag/AC were featureless with no evidence of $H_2$ uptake or release. This suggests formation of a metallic (Au and Ag) phase on AC in the as prepared samples, which is in line with

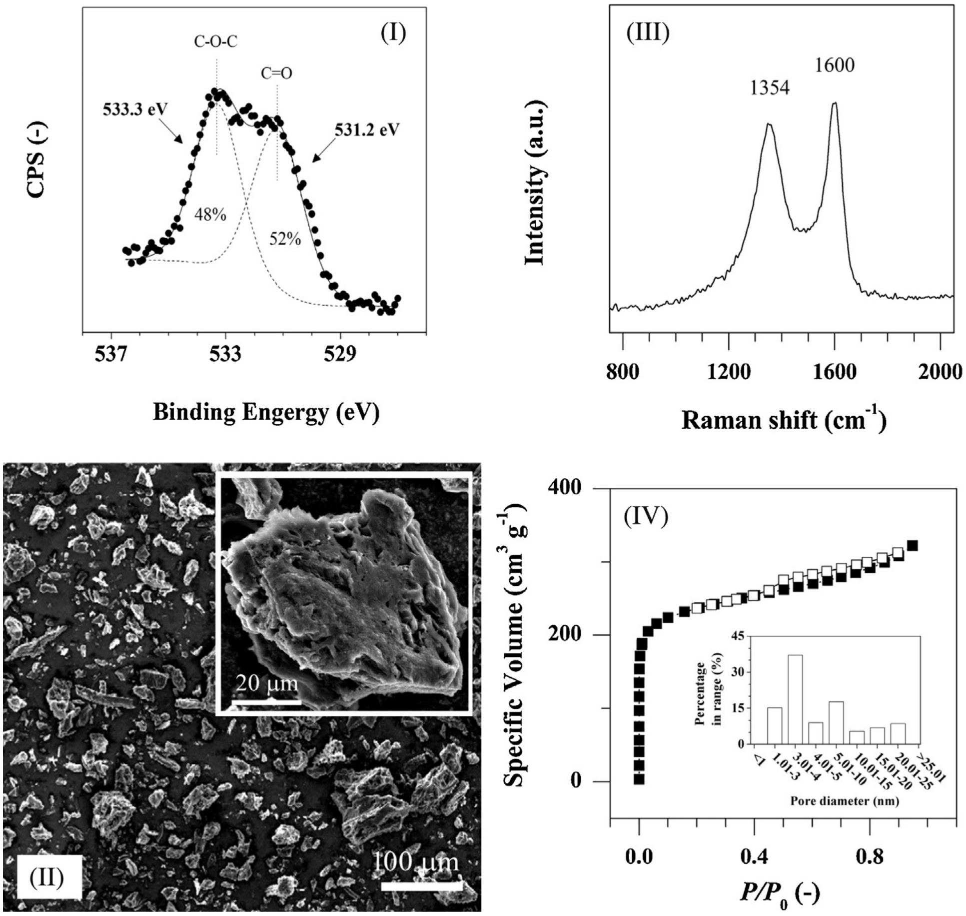

**Fig. 1.** **(I)** XPS spectrum over the O 1*s* region, **(II)** representative scanning electron microscopy (SEM) images, **(III)** Raman spectrum and **(IV)** $N_2$ adsorption (solid symbols)/desorption (open symbols) isotherms for acid treated AC with pore diameter distribution (see inset) from desorption measurements.

**Table 1**
Specific surface area (SSA), pore volume, metal loading, particle size range and mean (from XRD line broadening ($d_{hkl}$) and microscopy ($d$) analysis), $H_2$ chemisorbed (at 523 K)/released (during TPD), XPS binding energies and catalytic results (pseudo-first order rate constant ($k$) and turnover frequency (*TOF*)) associated with activated carbon (AC) support and 1 and 0.1%wt. Au and Ag catalysts.

| | | AC | 1%wt. Au/AC | 0.1%wt.Au/AC | 1%wt. Ag/AC | 0.1%wt. Ag/AC |
|---|---|---|---|---|---|---|
| SSA ($m^2 g^{-1}$) | | 518 | 635 | 605 | 694 | 585 |
| Pore volume ($cm^3$ $g^{-1}$) | | 0.34 | 0.48 | 0.44 | 0.57 | 0.53 |
| Metal loading (%wt.) | | – | 1 | 0.1 | 1 | 0.1 |
| $d_{hkl}$ (nm)[a,b] | | – | 12[a], 60[b] | 10[a], 12[b] | 13[a], 30[b] | 10[a], 12[b] |
| Metal particle size range (nm)[b] | | – | 25-60 | 1-15 | 3-20 | 1-9 |
| $d$ (nm)[b] | | – | 45 | 4 | 13 | 3 |
| $H_2$ uptake (mmol $g_{metal}^{-1}$)[b] | | – | 0.06 | 1.1 | 0.04 | 0.13 |
| TPD $H_2$ released ($cm^3$ $g^{-1}$)[b] | | – | 1.0 | 1.3 | 1.3 | 0.9 |
| XPS binding energies (eV)[b] | O 1s | 531.2<br>533.3 | – | – | – | – |
| | Au $4f_{7/2}$ | – | 84.0 | 83.6 | – | – |
| | Ag $3d_{5/2}$ | – | – | – | 368.3 | 368.0 |
| $k_{523K}$ ($h^{-1}$); *TOF* ($h^{-1}$) | | – | – | 126; 210 | – | 31; 39 |

[a] Samples as prepared.
[b] After thermal treatment to 623 K.

reports that have shown (by XPS [44] and EDX [45]) the occurrence of zero valent Au and Ag on acid-treated carbon supports. We should also note reported $H_2$ consumption (at 594 and 423 K) during TPR of Au/AC [40] and Ag/AC [46] where the AC carrier was not subjected to acid treatment. In the preparation of Au on carbon nanofibers Bulushev et al. [23] demonstrated that surface carboxylic groups decomposed during interaction with the $[Au(en)_2]Cl_3$ precursor with concomitant $Au^{3+}$ reduction to $Au^0$. Moreover, Jia and Demopoulos [47] proposed that surface hydroquinone species on $HNO_3$-treated AC were responsible for the reduction of $Ag^+$ (from $AgNO_3$ as precursor) to $Ag^0$. The SSA and total pore volume were increased after Au and Ag introduction (Table 1), an effect that was more pronounced at the higher loading (1%wt.). It has been shown that AC treatment with $HNO_3$ results in partial pore occlusion [48] where removal of the incorporated oxygen groups during thermal treatment (up to 573 K) served to increase surface area and pore volume [49].

The XRD profiles of Au/AC and Ag/AC are presented in Fig. 2 and show peaks characteristic of metallic Au ($2\theta = 38.1°, 44.4°, 64.7°$ and $77.5°$) or Ag ($2\theta = 38.1°, 44.3°, 64.4°$ and $77.5°$).

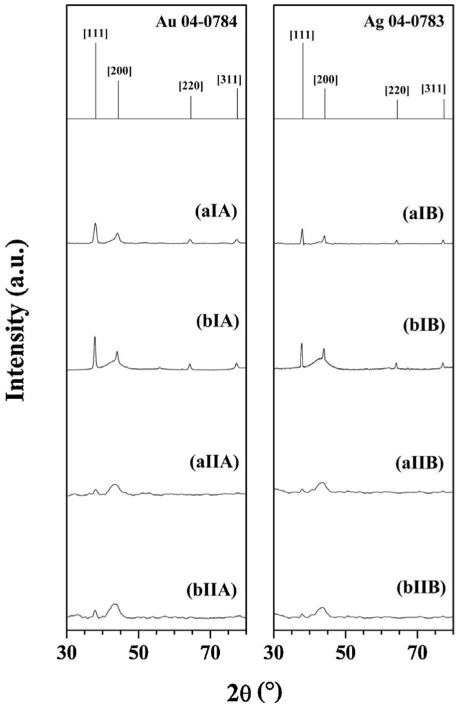

**Fig. 2.** XRD patterns associated with **(a)** as prepared and **(b)** activated **(I)** 1%wt. and **(II)** 0.1%wt. **(A)** Au/AC **(B)** and Ag/AC. JCPDS-ICDD reference diffractograms for Au (04-0784) and Ag (04-0783) are also included.

An XRD signal for metallic Au and Ag in the as prepared samples (**aIA, aIB, aIIA, aIIB**) confirms metal precursor reduction during synthesis as inferred from TPR analysis. Metal particle size from standard line broadening (Eq. (4)) was similar (10–13 nm) for the four as prepared catalysts. Thermal treatment (to 623 K) resulted in significant metal sintering at the 1%wt. loading which was not apparent at 0.1%wt.. Published work has shown a wider size range and formation of larger nanoparticles with increasing metal loading [20,50]. Metal particle size was further assessed by scanning and transmission electron microscopy and representative SEM **(I)** and TEM **(II)** images with associated metal particle size distributions **(III)** for activated 1%wt. Au **(A)** and Ag **(B)** are given in Fig. 3.

The supported metals are present as discrete nanoparticles with a quasi-spherical shape. Diffractogram patterns for isolated Au (not shown) and Ag (see inset to image **(IIB)**) particles confirmed the metal phase. Supported Au was characterised by a larger size range **(IIIA)**, suggesting stronger Ag-support interactions that limit agglomeration **(IIIB)**. Wang et al. [51] and Yang et al. [52] also reported the formation of larger Au nanocrystals (relative to Ag) on $TiO_2$ [51] and graphene oxide [52]. The 0.1%wt. loaded samples exhibit smaller particles, as can be assessed from the TEM images **(I–II)** in Fig. 4.

The diffractrogram patterns **(III)** are consistent with 0.24 and 0.20 nm *d*-spacings for (1 1 1) Au and (2 0 0) Ag. The TEM-generated size histograms Fig. 4**(IV)** establish a narrower size distribution with mean values that were close for Au (4 nm) and Ag (3 nm). Smaller particle size at lower loading agrees with the XRD line broadening measurement. The larger values obtained from the latter technique can be attributed to limitations of nanoparticle size measurement using the Scherrer formula where variations in metal size distribution can result in local modifications in the number of parallel lattice planes responsible for line broadening, resulting in over-estimation of size [53].

The catalytic response in hydrogenation over supported Au [54] and Ag [55] is influenced by geometric (metal particle size) and electronic (metal-support interactions) effects that can determine reactant adsorption/activation. XPS measurements were conducted to gain some insight into metal site electronic character and the resulting spectra over the Au 4*f* **(A)** and Ag 3*d* **(B)** BE regions associated with 1 **(I)** and 0.1 **(II)** %wt. loadings are given in Fig. 5.

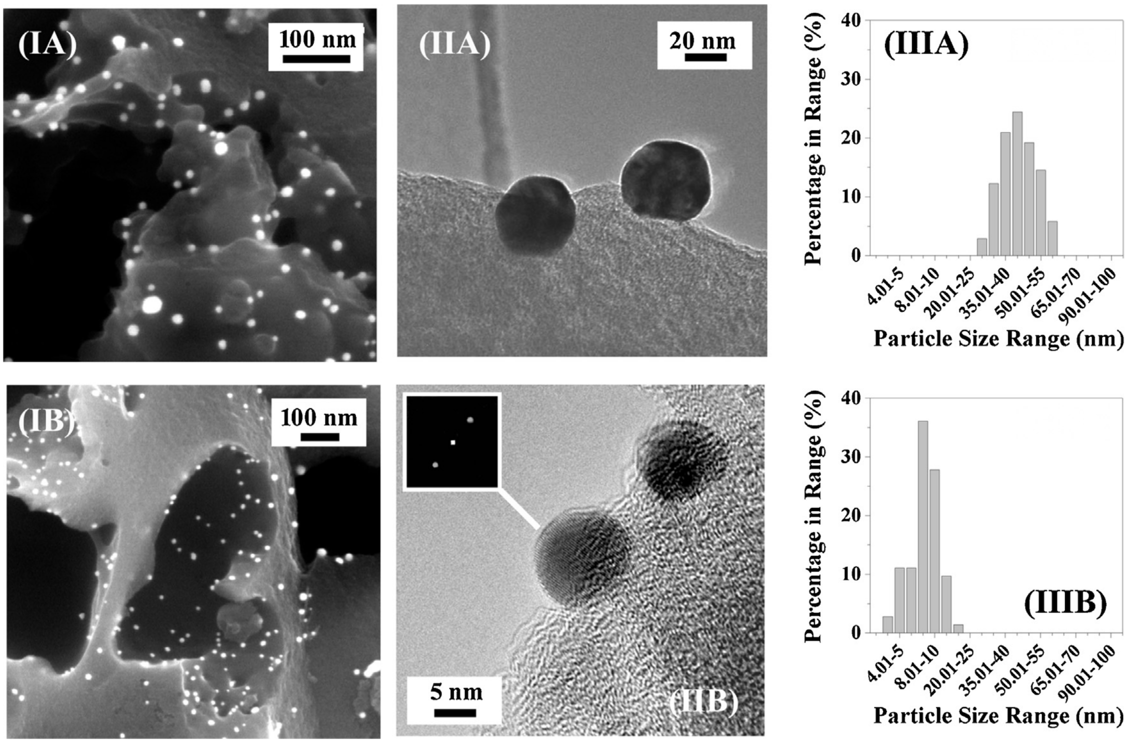

**Fig. 3.** Representative **(I)** SEM, **(II)** TEM images and **(III)** metal particle size distribution for activated 1%wt. **(A)** Au/AC and **(B)** Ag/AC. *Note*: Inset in **(IIB)** shows the diffractogram pattern for an isolated Ag particle.

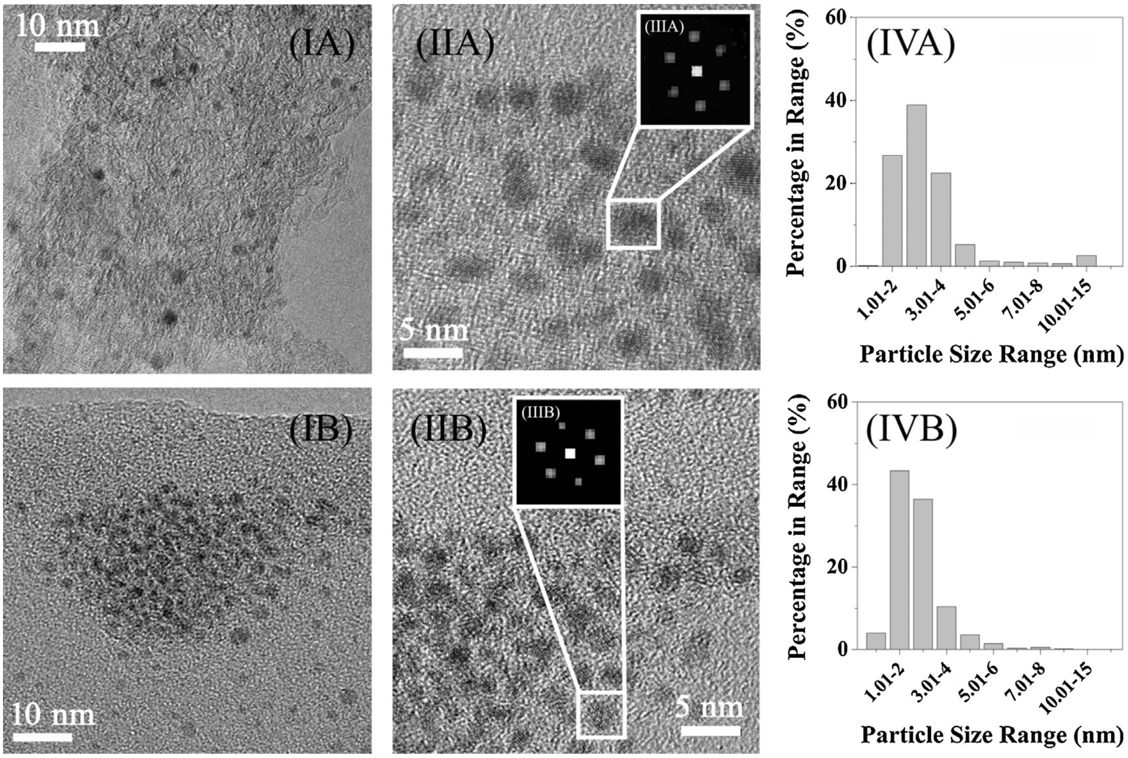

**Fig. 4.** Representative **(I)** medium and **(II)** high magnification TEM images with **(III)** diffractogram patterns for isolated metal particles and **(IV)** size distributions for activated 0.1%wt. **(A)** Au/AC and **(B)** Ag/AC.

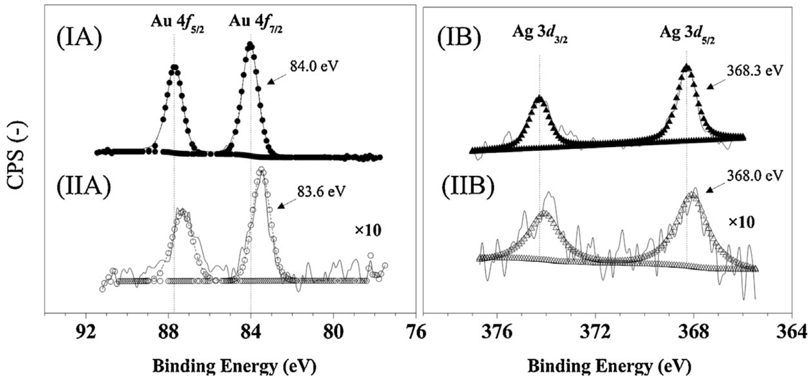

**Fig. 5.** XPS spectra over **(A)** Au 4*f* and **(B)** Ag 3*d* region associated with **(I)** 1%wt. (solid symbols) and **(II)** 0.1%wt. (open symbols) Au/AC (●,○) and Ag/AC (▲,△).

The core level Au $4f_{7/2}$ BE (84.0 eV) and Ag $3d_{5/2}$ (368.3 eV) for the higher loading are in good agreement with values reported in the literature for metallic Au [56] and Ag [57]. A decrease in peak intensity and increase in line width were observed at the lower loading as noted elsewhere [58] with a measurable shift to lower BE values (by 0.3–0.4 eV, see Table 1). Martínez et al. [59] investigating 1%wt. Au/$Fe_3O_4$ (9.0 nm, Au $4f_{7/2}$ BE = 83.8 eV) and Au/$SiO_2$ (5.7 nm, Au $4f_{7/2}$ BE = 82.6 eV) linked the downshift in BE to the formation of $Au^{\delta-}$ as a result of electron transfer from the support. It is known that surface functional groups with different electron-donating affinities can modify the electron density of supported metal nanoparticles [60]. Wang et al. demonstrated (by XAS) electron transfer from $HNO_3$ treated multi-walled carbon nanotubes (MWCNT) relative to untreated MWCNT and bulk Pt [61]. Such charge donation *via* AC oxygenated functionalities appears to apply to our lower loaded Au and Ag samples. While metal-support electron transfer can account for differences in the electronic properties of the supported metal phase in the low *vs.* high loaded samples, we should note possible charge transfer effects due to X-ray irradiation [62] and a contribution due to differences in metal particle size [63].

## 3.2. Catalyst performance

### 3.2.1. Catalyst activity

The gas phase hydrogenation of *m*-DNB over Au/C and Ag/AC at each loading was fully selective in terms of $-NO_2$ reduction with no evidence of hydrodenitrogenation and/or aromatic ring reduction. This result is significant as hydrogenolysis of substituted nitroarenes has been a feature of reaction over oxide supported Pd [64,65].

Hydrogenation was stable with time on-stream where, under the same reaction conditions, the lower metal loadings delivered significantly higher fractional conversion (Fig. 6). In contrast,

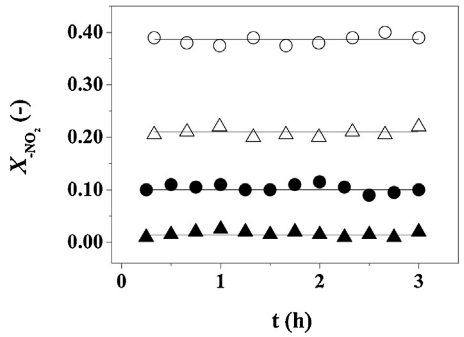

**Fig. 6.** Variation of –NO$_2$ fractional conversion ($X_{-NO_2}$) with time on-stream over 1%wt. (solid symbols) and 0.1%wt. (open symbols) Au/AC (●,○) and Ag/AC (▲,△). *Reaction conditions*: $T$ = 523 K, $P$ = 1 atm, $n/F = 1 \times 10^{-2}$ mol$_{metal}$ h mol$_{-NO_2}$$^{-1}$.

temporal deactivation in hydrogenation over oxide supported Au [29,66–69] and Ag [70] has been reported and attributed to coke formation [29,66], metal sintering [67,70] and reactant poisoning of active sites [68,69].

Given the higher conversions achieved we focused our attention on a comparison of 0.1%wt. Au/AC with Ag/AC. Nitro-group reduction can be quantified in terms of pseudo-first order kinetics [2]

$$\ln\left[\frac{1}{\left(1 - X_{-NO_2}\right)}\right] = k\left(\frac{n}{F}\right) \qquad (6)$$

where (n/F) has the physical meaning of contact time. The pseudo-first order rate constants were extracted from the plots in Fig. 7**(I)** and are recorded in Table 1. Comparison of intrinsic activity requires a measure of turnover frequency (*TOF*, hydrogenation rate per active site obtained from metal dispersion determined by microscopy [71]) where Au/AC delivered a greater than 5-fold higher *TOF* than Ag/AC. Oxide supported Au has been reported to outperform Ag in the hydrogenation of alkynes (1-hexyne [72]), esters (dimethyl oxalate [73]) and aldehydes (crotonaldehyde [74]). Enhanced activity for Au/AC extended over the 463–573 K range as demonstrated by the Arrhenius plots in Fig. 7**(II)** with an apparent activation energy of 110 kJ mol$^{-1}$ for *m*-DNB → *m*-NAN (Scheme 1) that is somewhat higher than the range of values (33-74 kJ mol$^{-1}$) reported for batch liquid phase hydrogenation of substituted nitroarenes (dinitrobenzene [75], dinitrotoluene [76], chloronitrobenzene [77] and nitrophenol [78]) over supported Pt [75,78], Ni [77] and Pd [76].

Hydrogen uptake/activation is a crucial parameter in catalytic hydrogenation [79]. It has been shown that spillover hydrogen (*i.e.* H$_2$ dissociation at a metal site with migration to the support [80]) can contribute to nitroarene hydrogenation activity [8,20,81]. Experimental and theoretical work have established that surface oxygen groups on carbon substrates serve to accommodate spillover hydrogen [79]. Total surface hydrogen was determined by TPD and the results are presented in Table 1 and Fig. 8.

The four samples exhibited H$_2$ desorption over the 645–873 K temperature range, which is comparable to results (623–873 K) reported for AC supported Pt [82], Pd [83,84] and Ni [83]. Release of hydrogen spillover has been shown to require temperatures in excess of 500 K regardless of the metal or carrier [85]. Total hydrogen desorbed from the four catalysts was similar (Table 1) suggesting that H$_2$ uptake during TPR was largely governed by the surface area and chemistry of the carrier. Chemisorption on supported Au [71] and Ag [86] is an activated process with increased uptake at higher temperatures. Hydrogen chemisorption capacity under reaction conditions (523 K) was appreciably higher at lower loadings (Table 1) and can be linked to facilitated dissociative chemisorption on edge/corner sites associated with smaller particles (<5 nm) [87]. The greater uptake on Au relative to Ag at the lower loading can account for the higher *m*-DNB hydrogenation rate.

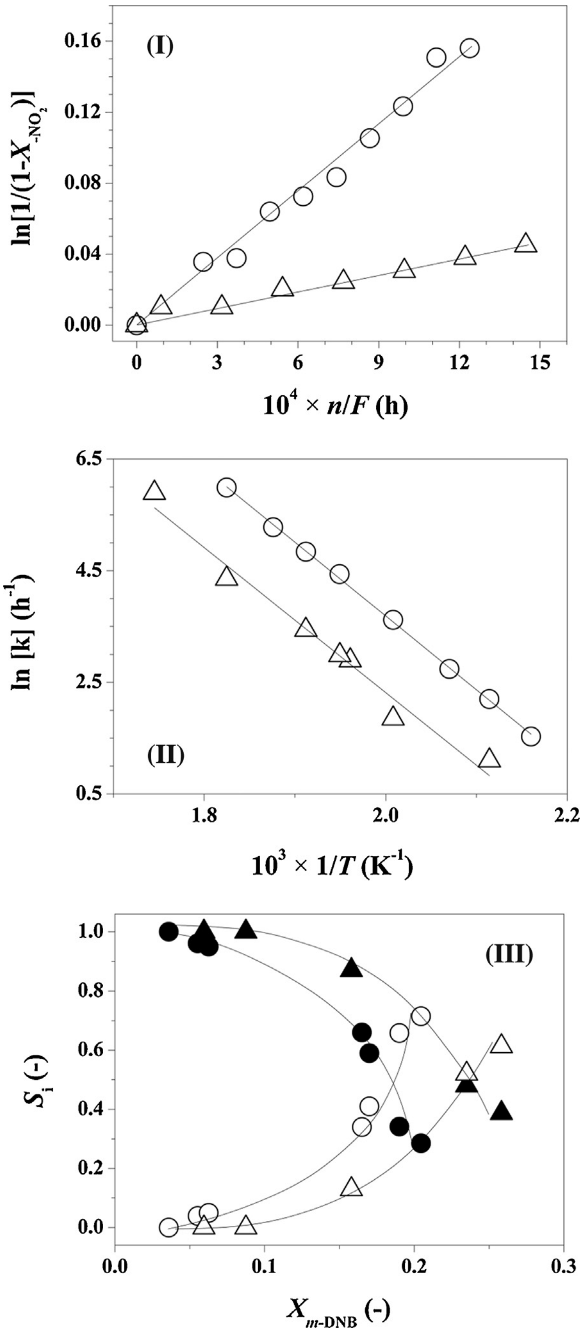

**Fig. 7.** **(I)** Pseudo-first order kinetic (*Reaction conditions*: $T$ = 523 K, $P$ = 1 atm) and **(II)** Arrhenius plots for the selective hydrogenation of *m*-DNB to *m*-NAN over 0.1%wt. Au/AC (○) and Ag/AC (△); **(III)** Variation of *m*-NAN (solid symbols) and *m*-PDM (open symbols) selectivity ($S_i$) with fractional conversion ($X_{m\text{-DNB}}$) over 0.1%wt. Au/AC (●,○) and Ag/AC (▲,△) (*Reaction conditions*: $T$ = 548 K, $P$ = 1 atm).

### 3.2.2. *Catalyst selectivity*

Full nitro-group reduction proceeds *via* stepwise and/or concerted routes (Scheme 1). The predominant pathway can be evaluated from a consideration of product (*m*-NAN and *m*-PDM) selectivity ($S_i$) as a function of *m*-DNB fractional conversion ($X_{m\text{-DNB}}$) and the results over the two low loaded catalysts are given in Fig. 7**(III)**. Exclusivity in terms of partial –NO$_2$ reduction to *m*-NAN at low fractional conversions (<0.06) over both cata-

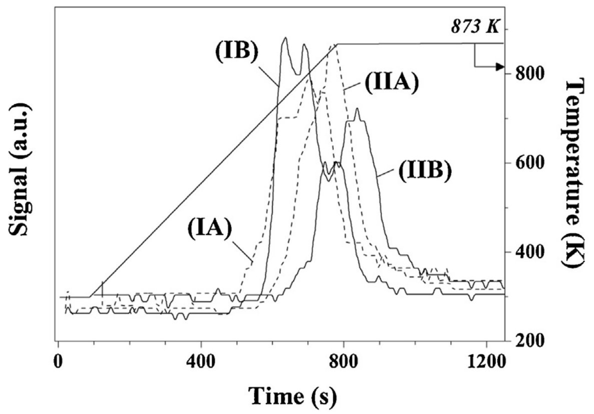

**Fig. 8.** Hydrogen TPD profiles generated for: **(I)** 1%wt. and **(II)** 0.1%wt. **(A)** Au/AC (dashed lines) and **(B)** Ag/AC (solid lines).

lysts suggests an analogous reaction mechanism where nitro-group reduction occurs predominantly in a stepwise fashion (paths **(I, II)** in Scheme 1). We should note that catalytic systems reported to date have promoted the formation of both (*m*-NAN and *m*-PDM) products where high temperatures and/or pressures were identified as essential to achieve high selectivities to *m*-NAN. Zhao et al. [88] reported 97% selectivity to *m*-NAN over 5%wt. Pt/C (at 160 bar) while selectivities >80% were recorded for reaction (at $P_{H_2}$ up to 45 bar) over Pd/C [25] and Ru/$Al_2O_3$ [89]. In this work, full selectivity to *m*-NAN was attained over Au/C and Au/Ag at ambient pressure. Selectivity to *m*-PDM was favoured at increasing conversion. Consecutive formation of *m*-NAN and *m*-PDM has been reported for batch liquid reaction over Pt/$TiO_2$ [75] and carbon supported Ni [26] and Ni-Pt [26]. Distinct differences in selectivity are in evidence for the two metals at higher conversions where a preferential formation of *m*-NAN was observed over Ag/AC. This suggests a deviation in *m*-DNB adsorption-activation mechanism for both systems. *m*-DNB adsorption on $Au^{\delta-}$ (from XPS) through the benzene ring results in repulsion between the $\pi$-delocalized electrons and the charged gold nanoparticles [8]. This generates a resonance structure with two positive localised charges on the ring where both –$NO_2$ groups are activated with the formation of *m*-PDM *via* nucleophilic attack. A preferential interaction through the -$NO_2$ function on supported Ag in functionalised nitroarenes has been demonstrated by surface-enhanced Raman scattering (SERS) [90,91]. This results in a resonance structure with a single delocalised positive charge on the ring and only one –$NO_2$ group is activated, favouring *m*-NAN production.

## 4. Conclusions

Acid ($HNO_3 + H_2SO_4$) treatment of an amorphous carbon support incorporated carbonyl and carboxyl anhydride groups (from acid-base titration and XPS) that facilitate Au and Ag deposition. Thermal activation of 1%wt. Au/AC and Ag/AC to 623 K generated a broad metal particle size distribution (25–60 nm Au, mean = 45 nm, 3–20 nm Ag, mean = 13 nm) with XPS BE values close to the reference metals. A decrease in metal loading (1 → 0.1%wt.) resulted in a narrower distribution of smaller supported Au (1–15 nm, mean = 4 nm) and Ag (1–9 nm, mean = 3 nm) nanoparticles with evidence (from XPS) of charge transfer from the support. The supported Au and Ag catalysts exhibited stable *m*-DNB hydrogenation activity with time on-stream and an equivalent apparent activation energy (110 kJ $mol^{-1}$) for selective partial hydrogenation of *m*-DNB to *m*-NAN. Au/AC delivered a (5-fold) higher specific hydrogenation rate than Ag/AC, which can be attributed to greater $H_2$ chemisorption under reaction conditions. The conversion/selectivity patterns are consistent with sequential transformation of *m*-DNB to *m*-NAN at low conversions and a switch to full hydrogenation to *m*-PDM at higher conversion. Selectivity to *m*-NAN was measurably higher over Ag/AC, which we attribute to differences in *m*-DNB adsorption/activation. We have provided an explicit comparison of the chemoselective hydrogenation response of Au/AC and Ag/AC and demonstrate that supported Au exhibits a higher intrinsic hydrogenation rate linked to elevated $H_2$ uptake where selectivity to *m*-NAN is greater on Ag.

## Acknowledgements

This work was financially supported by the Swiss National Science Foundation. The authors are grateful to Pedro Benavente-Donayre and Dr. Antonio Nieto-Márquez for their contributions.

## References

[1] P. Lara, K. Philippot, Catal. Sci. Technol. 4 (2014) 2445–2465.
[2] F. Cárdenas-Lizana, M.A. Keane, in: L. Prati, A. Villa (Eds.), Gold Catalysis: Preparation, Characterization and Applications in the Gas and Liquid Phase, Pan Stanford Publ, Singapore, 2014.
[3] M. Pietrowski, Curr. Org. Synth. 9 (2012) 470–487.
[4] X. Wang, F. Cárdenas-Lizana, M.A. Keane, ACS Sust. Chem. Eng. 2 (2014) 2781–2789.
[5] F. Cárdenas-Lizana, C. Berguerand, I. Yuranov, L. Kiwi-Minsker, J. Catal. 301 (2013) 103–111.
[6] F. Cárdenas-Lizana, M.A. Keane, J. Mat. Sci. 48 (2013) 543–564.
[7] F. Cárdenas-Lizana, Z. Martínez de Pedro, S. Gómez-Quero, M.A. Keane, J. Mol. Catal. 326 (2010) 48–54.
[8] F. Cárdenas-Lizana, S. Gómez-Quero, N. Perret, M.A. Keane, Catal. Sci. Technol. 1 (2011) 652–661.
[9] X. Wang, N. Perret, J.J. Delgado, G. Blanco, X. Chen, C.M. Olmos, S. Bernal, M.A. Keane, J. Phys. Chem. C 117 (2013) 994–1005.
[10] F. Rodríguez-Reinoso, Carbon 36 (1998) 159–175.
[11] T. Szumełda, A. Drelinkiewicz, R. Kosydar, J. Gurgul, Appl. Catal. A: Gen. 487 (2014) 1–15.
[12] H. Gu, X. Xu, A.-A. Chen, P. Ao, X. Yan, Catal. Commun. 41 (2013) 65–69.
[13] M. Bonarowska, Z. Kaszkur, D. Łomot, M. Rawski, Z. Karpiński, Appl. Catal. B: Environ. 162 (2015) 45–56.
[14] M. Lu, J. Sun, D. Zhang, M. Li, J. Zhu, Y. Shan, Reac. Kinet. Mech. Cat. 100 (2010) 99–103.
[15] X. Zhang, Y.C. Guo, Z.C. Zhang, J.S. Gao, C.M. Xu, J. Catal. 292 (2012) 213–226.
[16] B. Li, H. Li, Z. Xu, J. Phys. Chem. C 113 (2009) 21526–21530.
[17] M. Lu, X. Li, B. Chen, M. Li, H. Xin, L. Song, J. Nanosci. Nanotechnol. 14 (2014) 7315–7318.
[18] X. Yang, Y. Liang, X. Zhao, Y. Song, L. Hu, X. Wang, Z. Wang, J. Qiu, RSC Adv. 4 (2014) 31932–31936.
[19] L. Prati, A. Villa, A.R. Lupini, G.M. Veith, Phys. Chem. Chem. Phys. 14 (2012) 2969–2978.
[20] F. Cárdenas-Lizana, M.A. Keane, Phys. Chem. Chem. Phys. (2015), http://dx.doi.org/10.1039/C5CP00282F, in press.
[21] F. Cárdenas-Lizana, Y. Hao, M. Crespo-Quesada, I. Yuranov, X. Wang, M.A. Keane, L. Kiwi-Minsker, ACS Catal. 3 (2013) 1386–1396.
[22] D.S. Cameron, S.J. Cooper, I.L. Dodgson, B. Harrison, J.W. Jenkins, Catal. Today 7 (1990) 113–137.
[23] D.A. Bulushev, I. Yuranov, E.I. Suvorova, P.A. Buffat, L. Kiwi-Minsker, J. Catal. 224 (2004) 8–17.
[24] K.A. Wepasnick, B.A. Smith, K.W. Schrote, H.K. Wilson, S.R. Diegelmann, D.H. Fairbrother, Carbon 49 (2011) 24–36.
[25] V.L. Khilnani, S.B. Chandalia, Org. Proc. Res. Dev. 5 (2001) 263–266.
[26] M.M. Telkar, J.M. Nadgeri, C.V. Rode, R.V. Chaudhari, Appl. Catal. A: Gen. 295 (2005) 23–30.
[27] X. Bokhimi, R. Zanella, V. Maturano, A. Morales, Mater. Chem. Phys. 138 (2013) 490–499.
[28] M. Khoudiakov, M.C. Gupta, S. Deevi, Appl. Catal. A: Gen. 291 (2005) 151–161.
[29] F. Cárdenas-Lizana, X. Wang, D. Lamey, M. Li, M.A. Keane, L. Kiwi-Minsker, Chem. Eng. J. 255 (2014) 695–704.
[30] C. Amorim, M.A. Keane, J. Chem. Technol. Biotechnol. 83 (2008) 662–672.
[31] G.-M. Choi, T. Ohmi, J. Electrochem. Soc. 148 (2001) G241–G248.
[32] S. Santangelo, G. Messina, G. Faggio, S.H.A. Rahim, C. Milone, J. Raman Spectrosc. 43 (2012) 1432–1442.
[33] M.K. van der Lee, J. van Dillen, J.H. Bitter, K.P. de Jong, J. Am. Chem. Soc. 127 (2005) 13573–13582.
[34] U. Zielke, K.J. Hüttinger, W.P. Hoffman, Carbon 34 (1996) 983–998.
[35] J.L. Figueiredo, M.F.R. Pereira, M.M.A. Freitas, J.J.M. Órfão, Carbon 37 (1999) 1379–1389.
[36] H. Marsh, F. Rodríguez-Reinoso, Activated Carbon, Elsevier, Amsterdam, 2006.
[37] S. Choi, K.H. Park, S. Lee, K.H. Koh, J. Appl. Phys. 92 (2002) 4007–4011.

[38] M.S. Dresselhaus, G. Dresselhaus, R. Saito, A. Jorio, Phys. Rep. -Rev. Sec. Phys. Lett. 409 (2005) 47–99.
[39] T. Maiyalagan, B. Viswanathan, Mater. Chem. Phys. 93 (2005) 291–295.
[40] S. Gil, L. Muñoz, L. Sánchez-Silva, A. Romero, J.L. Valverde, Chem. Eng. J. 172 (2011) 418–429.
[41] P. Kim, Y.Z. Zheng, S. Agnihotri, Ind. Eng. Chem. Res. 47 (2008) 3170–3178.
[42] A.H. El-Sheikh, A.P. Newman, H.K. Al-Daffaee, S. Phull, N. Cresswell, J. Anal. Appl. Pyrolysis 71 (2004) 151–164.
[43] M. Thommes, Chem. Ing. Tech. 82 (2010) 1059–1073.
[44] Y. Gu, X. Hou, H. Hu, B. Yu, L. Wang, F. Zhou, Mater. Chem. Phys. 116 (2009) 284–288.
[45] J.S. Hoskins, T. Karanfil, S.M. Serkiz, Environ. Sci.Technol. 36 (2002) 784–789.
[46] L. Chen, D. Ma, X. Bao, J. Phys. Chem. C 111 (2007) 2229–2234.
[47] Y. Jia, G.P. Demopoulos, Ind. Eng. Chem. Res. 42 (2002) 72–79.
[48] J. Li, L. Ma, X. Li, C. Lu, H. Liu, Ind. Eng. Chem. Res. 44 (2005) 5478–5482.
[49] G.S. Szymański, Z. Karpiński, S. Biniak, A. Świątkowski, Carbon 40 (2002) 2627–2639.
[50] S.H. Overbury, V. Schwartz, D.R. Mullins, W. Yan, S. Dai, J. Catal. 241 (2006) 56–65.
[51] Y.M. Wang, G.J. Du, H. Liu, D. Liu, S.B. Qin, J.Y. Wang, X.T. Tao, M.H. Jiang, Z.L. Wang, J. Nanosci. Nanotechnol. 9 (2009) 2119–2123.
[52] M.-Q. Yang, X. Pan, N. Zhang, Y.-J. Xu, CrystEngComm 15 (2013) 6819–6828.
[53] H. Borchert, E.V. Shevchenko, A. Robert, I. Mekis, A. Kornowski, G. Grübel, H. Weller, Langmuir 21 (2005) 1931–1936.
[54] M. Boronat, P. Concepción, A. Corma, S. González, F. Illas, P. Serna, J. Am. Chem. Soc. 129 (2007) 16230–16237.
[55] G. Vilé, D. Baudouin, I.N. Remediakis, C. Copéret, N. López, J. Pérez-Ramírez, ChemCatChem 5 (2013) 3750–3759.
[56] S. Peters, S. Peredkov, M. Neeb, W. Eberhardt, M. Al-Hada, Surf. Sci. 608 (2013) 129–134.
[57] E. Sumesh, M.S. Bootharaju, Anshup, T. Pradeep, J. Hazard. Mater. 189 (2011) 450–457.
[58] W. Grünert, Characterization of Solid Materials and Heterogeneous Catalysts: From Structure to Surface Reactivity, in: M. Che, J.C. Védrine (Eds.), Wiley-VCH, Weinheim, 2012.
[59] J.J. Martínez, H. Rojas, L. Vargas, C. Parra, M.H. Brijaldo, F.B. Passos, J. Mol. Catal. A: Chem. 383–384 (2014) 31–37.
[60] J. Zhu, A. Holmen, D. Chen, ChemCatChem 5 (2013) 378–401.
[61] X. Wang, N. Li, J.A. Webb, L.D. Pfefferle, G.L. Haller, Appl. Catal. B: Environ. 101 (2010) 21–30.
[62] N. Kruse, S. Chenakin, Appl. Catal. A: Gen. 391 (2011) 367–376.
[63] J.T. Miller, A.J. Kropf, Y. Zha, J.R. Regalbuto, L. Delannoy, C. Louis, E. Bus, J.A. van Bokhoven, J. Catal. 240 (2006) 222–234.
[64] T.T. Bovkun, M. Grayevsky, Y. Sasson, J. Blum, J. Mol. Catal. A: Chem. 270 (2007) 171–176.
[65] F. Cárdenas-Lizana, S. Gómez-Quero, C. Amorim, M.A. Keane, Appl. Catal. A: Gen. 473 (2014) 41–50.
[66] Y. Azizi, C. Petit, V. Pitchon, J. Catal. 256 (2008) 338–344.
[67] X. Zhang, H. Shi, B.-Q. Xu, Catal. Today 122 (2007) 330–337.
[68] R. Zanella, C. Louis, S. Giorgio, R. Touroude, J. Catal. 223 (2004) 328–339.
[69] J.A. Lopez-Sanchez, D. Lennon, Appl. Catal. A: Gen. 291 (2005) 230–237.
[70] M. Bron, D. Teschner, A. Knop-Gericke, F.C. Jentoft, J. Kröhnert, J. Hohmeyer, C. Volckmar, B. Steinhauer, R. Schlögl, P. Claus, Phys. Chem. Chem. Phys. 9 (2007) 3559–3569.
[71] M. Li, X. Wang, N. Perret, M.A. Keane, Catal. Commun. 46 (2014) 187–191.
[72] G. Vilé, J. Pérez-Ramírez, Nanoscale 6 (2014) 13476–13482.
[73] J. Zheng, H. Lin, Y.-N. Wang, X. Zheng, X. Duan, Y. Yuan, J. Catal. 297 (2013) 110–118.
[74] X. Yang, A. Wang, X. Wang, T. Zhang, K. Han, J. Li, J. Phys. Chem. C 113 (2009) 20918–20926.
[75] H. Rojas, G. Borda, M. Brijaldo, P. Reyes, J. Valencia, Reac. Kinet. Mech. Catal. 105 (2012) 271–284.
[76] G. Neri, M.G. Musolino, C. Milone, S. Galvagno, Ind. Eng. Chem. Res. 34 (1995) 2226–2231.
[77] Y.-Z. Chen, Y.-C. Chen, Appl. Catal. A: Gen. 115 (1994) 45–57.
[78] X. Li, G. Li, W. Zang, L. Wang, X. Zhang, Catal. Sci. Technol. 4 (2014) 3290–3297.
[79] R. Prins, Chem. Rev. 112 (2012) 2714–2738.
[80] R. Prins, V.K. Palfi, M. Reiher, J. Phys. Chem. C 116 (2012) 14274–14283.
[81] F. Cárdenas-Lizana, S. Gómez-Quero, C.J. Baddeley, M.A. Keane, Appl. Catal. A: Gen. 387 (2010) 155–165.
[82] A. Huidobro, A. Sepúlveda-Escribano, F. Rodríguez-Reinoso, in: A. Guerrero-Ruíz, I. Rodríguez-Ramos (Eds.), Studies in Surface Science and Catalysis, Vol. 138, Elsevier, Amsterdam, 2001, pp. 275–283.
[83] C. Amorim, X. Wang, M.A. Keane, Chin. J. Catal. 32 (2011) 746–755.
[84] C. Amorim, G. Yuan, P.M. Patterson, M.A. Keane, J. Catal. 234 (2005) 268–281.
[85] C. Amorim, M.A. Keane, J. Hazard. Mater. 211–212 (2012) 208–217.
[86] J. Hohmeyer, E.V. Kondratenko, M. Bron, J. Kröhnert, F.C. Jentoft, R. Schlögl, P. Claus, J. Catal. 269 (2010) 5–14.
[87] E. Bus, J.T. Miller, J.A. van Bokhoven, J. Phys. Chem. B 109 (2005) 14581–14587.
[88] F. Zhao, S.-I. Fujita, J. Suna, Y. Ikushima, M. Arai, Catal. Today 98 (2004) 523–528.
[89] S. Zhao, H. Liang, Y. Zhou, Catal. Commun. 8 (2007) 1305–1309.
[90] V. Chiş, M.M. Venter, N. Leopold, O. Cozar, Vib. Spectrosc. 48 (2008) 210–214.
[91] M. Muniz-Miranda, Appl. Catal. B: Environ. 146 (2014) 147–150.